2024

Clusters, Clumps, Dust, and Gas (CCDG) in NGC 1614: Benchmarking Cluster Demographics in Extreme Systems

Caputo, Miranda, Chandar, Rupali, Mok, Angus, Linden, Sean, Goudfrooij, Paul and Whitmore, Bradley C.

The Astronomical Journal, 168:259 (15pp), 2024 December https://doi.org/10.3847/1538-3881/ad7de7

Clusters, Clumps, Dust, and Gas (CCDG) in NGC 1614: Benchmarking Cluster Demographics in Extreme Systems

Miranda Caputo[1], Rupali Chandar[1], Angus Mok[2], Sean Linden[3], Paul Goudfrooij[4], and Bradley C. Whitmore[4]
[1] Ritter Astrophysical Research Center, University of Toledo, Toledo, OH 43606, USA; Miranda.Caputo@rockets.utoledo.edu
[2] OCAD University, Toronto, ON M5T 1W1, Canada
[3] Steward Observatory, University of Arizona, 933 N. Cherry Avenue, Tucson, AZ 85721, USA
[4] Space Telescope Science Institute, 3700 San Martin Drive, Baltimore, MD 21218, USA
Received 2024 April 5; revised 2024 August 29; accepted 2024 September 20; published 2024 November 13

Abstract

Observations of young star clusters in a variety of galaxies have been used to constrain basic properties related to star formation, such as the fraction of stars found in clusters (Γ) and the shape of the cluster mass function (CMF). However, the results can depend heavily on the reliability of the cluster age-dating process and other assumptions. One of the biggest challenges for successful age-dating lies in breaking the age–reddening degeneracy, where older, dust-free clusters and young, reddened clusters can have similar broadband colors. While this degeneracy affects cluster populations in all galaxies, it is particularly challenging in systems with dusty, extreme star-forming environments. We study the cluster demographics in the luminous infrared galaxy NGC 1614 using Hubble Space Telescope imaging taken in eight optical–near-infrared passbands. For age-dating, we adopt a spectral energy distribution fitting process that limits the maximum allowed reddening by region and includes Hα photometry directly. We find that without these assumptions essentially all clusters in the dust-free UV-bright arm that should have ages ≈50–250 Myr are incorrectly assigned ages younger than 10 Myr. We find that this method greatly reduces the number of clusters in the youngest ($\tau < 10$ Myr) age bin and shows a fairly uniform distribution of massive clusters, the most massive being ≈few $\times 10^7\,M_\odot$. A maximum likelihood fit shows that the CMF is well fitted by a power law with an index of approximately −1.8, with no statistically significant high-mass cutoff. We calculate the fraction of stars born in clusters to be $\Gamma_{1-10} = 22.4\% \pm 5.7\%$. The fraction of stars in clusters decreases quickly over time, with $\Gamma_{10-100} = 4.5\% \pm 1.1\%$ and $\Gamma_{100-400} = 1.7\% \pm 0.4\%$, suggesting that clusters dissolve rapidly over the first ∼0.5 Gyr. The decreasing fraction of stars in clusters is consistent with the declining shape observed for the cluster age distribution.

Unified Astronomy Thesaurus concepts: Luminous infrared galaxies (946); Star clusters (1567)

1. Introduction

Extremely massive star clusters (∼10^6–$10^8\,M_\odot$), which may be young analogs of ancient globular clusters, are forming in extreme star-forming galaxies in the nearby (<100 Mpc) universe (S. F. Portegies Zwart et al. 2010; S. T. Linden et al. 2017; A. Adamo et al. 2020). The star formation in many of these systems is triggered by minor or major merging events between gas-rich galaxies, which can lead to an infrared-luminous phase. Nearby merging systems give important insight into the star and cluster formation processes that operated near cosmic noon, $z \sim 1.5$–3, when merging was much more common than in the modern universe (e.g., C. R. Bridge et al. 2007; C. J. Conselice 2014; A. Carpineti et al. 2015).

Studying intensely star-forming galaxies, where the star formation rate (SFR) is $>2\sigma$ above the star-forming main sequence (e.g., J. S. Speagle et al. 2014), allows us to probe the high end of fundamental relationships that may depend on SFR (in $M_\odot\,\mathrm{yr}^{-1}$) or SFR density ($\Sigma_{\rm SFR}$ in $M_\odot\,\mathrm{yr}^{-1}\,\mathrm{kpc}^{-2}$). One example is the cluster mass function (CMF), which encodes important information about the formation and evolution of cluster populations in galaxies. Most current simulations either find or assume that the CMF has a Schechter-like distribution, with an upper mass cutoff that increases with $\Sigma_{\rm SFR}$ of the galaxy (H. Li et al. 2017, 2018). Observational works find somewhat mixed results for the shape of the CMF, with some favoring a Schechter-like distribution (S. F. Portegies Zwart et al. 2010; N. Bastian et al. 2012; L. C. Johnson et al. 2017; M. Messa et al. 2018; A. Adamo et al. 2020) and others finding that a single power-law fits the observations well (B. C. Whitmore et al. 2010; R. Chandar et al. 2014, 2016, 2023b; D. O. Cook et al. 2019; A. Adamo et al. 2020).

Another parameter that may vary with SFR and $\Sigma_{\rm SFR}$ is the fraction of stars found in clusters, Γ. We assume that the fraction of stars found in 1–10 Myr clusters is a good proxy for the fraction *born* in clusters. A number of observational works have suggested that the fraction of stars found in clusters with ages between 1 and 10 Myr increases with $\Sigma_{\rm SFR}$ (Q. E. Goddard et al. 2010; A. Adamo et al. 2015, 2020; L. C. Johnson et al. 2016) from just a few percent to nearly 100%. However, this result has been called into question owing to clusters of different ages being used to estimate Γ in galaxies with low versus high $\Sigma_{\rm SFR}$ (R. Chandar et al. 2017). Newer works suggest that potential issues with cluster age-dating may also have affected previous results for Γ (R. Chandar et al. 2023b).

One key challenge in determining the shape of the CMF and in calculating Γ in nearby star-forming galaxies arises from the difficulty of breaking the age–reddening degeneracy of clusters in these dusty systems based on broadband measurements alone. One improvement is to include Hα in the age-dating procedure, as B. C. Whitmore et al. (2020) did to improve

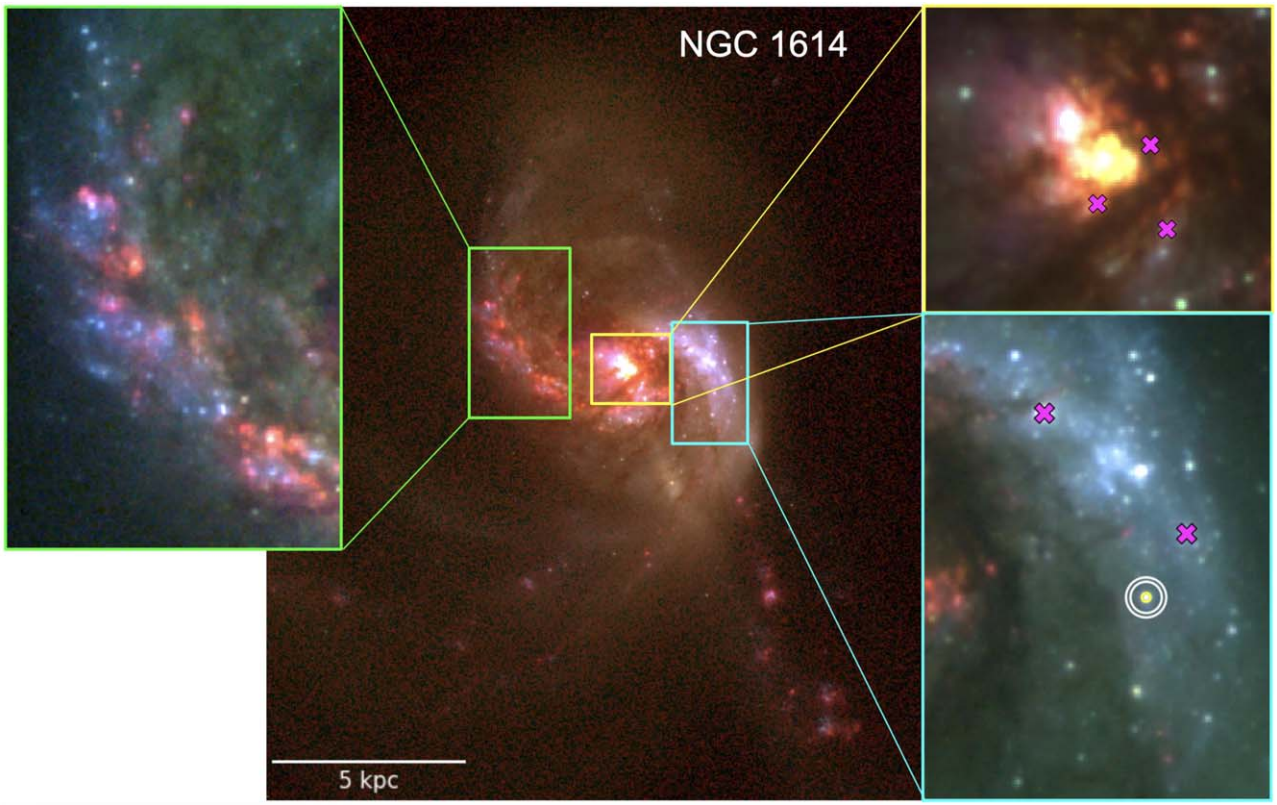

Figure 1. HST image of NGC 1614, with B, V, and Hα represented by blue, green, and red, respectively. A variety of environments within this galaxy are highlighted, with the western UV-bright arm, eastern star-forming arm, and central region enlarged as shown. The yellow circle represents an aperture with a 2-pixel radius. The white circles show the 7- and 9-pixel radii used to determine the background level. The locations of the five most massive clusters younger than 400 Myr are shown as the magenta crosses in the two right panels.

cluster ages in the dwarf starburst galaxy NGC 4449. Recently, B. C. Whitmore et al. (2023a) found that ancient globular clusters in nearby spiral galaxies were being assigned ages that are too young by factors of 10–1000, but that including Hα or CO information significantly improved the age-dating results for globular clusters. R. Chandar et al. (2023a, 2023b) found that including Hα measurements, combined with limiting the maximum allowed $E(B-V)$ in the spectral energy distribution (SED) fitting, improved the resulting ages and, in particular, reduced the number of clusters incorrectly dated to ages younger than 10 Myr.

In this work we will focus on the cluster population in NGC 1614, which was observed as a part of the Clusters, Clumps, Dust, and Gas (CCDG) multiband Hubble Space Telescope (HST) imaging survey of 13 extreme star-forming galaxies. NGC 1614 (Figure 1) is a minor merger between a spiral and a dwarf galaxy, is located at $D \sim 69.7$ Mpc, and is a luminous infrared galaxy (LIRG; $L_{\rm IR}/L_{\odot} = 11.6$). NGC 1614 has a variety of environments, including tidal tails, a star-forming dusty arm in the west, a nearly dust-free UV-bright arm in the east (similar to UV-bright clumps observed in galaxies at $z \sim 1$–2), and a dust-enshrouded central region. Active galactic nucleus (AGN) activity has not been detected from the center of NGC 1614 (R. Herrero-Illana et al. 2017). Due to these different environments that have different amounts of dust, NGC 1614 is a good target for testing assumptions related to reddening ($E(B-V)$) during the age-dating process.

The remainder of this paper is organized as follows: Section 2 looks at the properties of NGC 1614 and presents the HST data with source detection in the optical and a few clusters discovered in the near-infrared (NIR) imaging. Section 3 focuses on cluster analysis and methods to handle the age–reddening degeneracy. Section 4 presents the results found for the cluster age and mass estimates, CMFs, age distributions, and Γ. We discuss the physical implications in Section 5. Section 6 gives a summary of our conclusion, and in the Appendix we discuss uncertainties in the assumptions used to calculate Γ and implications for published results in NGC 1614 and other galaxies.

2. NGC 1614: Properties, Observations, and Cluster Catalog

2.1. Star Formation Rate

In this paper, we aim to understand the relationship between star and star cluster formation in NGC 1614. In order to do this, we establish the SFR and SFR per unit area ($\Sigma_{\rm SFR}$) that we will use for NGC 1614 in this section.

NGC 1614 has had several SFR estimates over the past decade using a variety of tracers, including hydrogen recombination lines tracing very recent ($\tau \leqslant 10$ Myr) star formation and infrared luminosity that includes emission from older ($\tau \approx$ few $\times$ 100 Myr) populations (E. J. Murphy et al. 2012).

Some previously estimated SFRs from hydrogen lines for NGC 1614 include (1) 27.4 $M_{\odot}\,{\rm yr}^{-1}$, based on HST continuum-subtracted Hα emission corrected for the median extinction found from young clusters (A. Adamo et al. 2020); (2) 49.6 $M_{\odot}\,{\rm yr}^{-1}$, from HST Paβ emission after applying a dust

correction using the Balmer-to-Paschen decrement (Hα/Paβ) (C. Giménez-Arteaga et al. 2022); and (3) 74.7 $M_\odot$ yr^{-1}, from dust-extinction-corrected Paα emission (K. Tateuchi et al. 2015).

IR emission tends to trace stellar populations that have ages up to ∼500 Myr (R. C. Kennicutt & N. J. Evans 2012). For NGC 1614, IR-based SFR estimates include (1) from 41.8 $M_\odot$ yr^{-1}, based on F110W luminosity from HST, to 95.7 $M_\odot$ yr^{-1}, when 24 μm flux is included (C. Giménez-Arteaga et al. 2022); (2) 49.0 $M_\odot$ yr^{-1}, based on 8–1000 μm emission (K. Tateuchi et al. 2015); and (3) 51.3 $M_\odot$ yr^{-1}, from IRAS IR data (S. T. Linden et al. 2017).

While there is a range in published SFR estimates for both the hydrogen line and IR emission, there is reasonable agreement between estimates that use these two tracers, which give an average of ∼51 and ∼59 $M_\odot$ yr^{-1} for hydrogen lines and IR emission, respectively. This suggests that the SFR has been fairly constant over at least the past ∼100 Myr, and likely ≈0.5 Gyr. In this work, we adopt an SFR for NGC 1614 of 49.6 $M_\odot$ yr^{-1} from C. Giménez-Arteaga et al. (2022) based on hydrogen recombination lines, since they trace the most recent (<10 Myr) star formation. This rate is quite similar to the mean values found between the different published results for hydrogen lines and from IR emission. We adopt an uncertainty of 25% following D. O. Cook et al. (2023) and R. Chandar et al. (2023b).

We estimate the area of NGC 1614 to be ∼200 kpc^{-2}. This region includes essentially all of the clusters in our sample plus parts of the tidal tails to the south, east, and north. With our adopted SFR of 49.6 $M_\odot$ yr^{-1} and area of 200 kpc^2, $\Sigma_{\rm SFR} = 0.25\ M_\odot$ yr^{-1} kpc^{-2}. A. Adamo et al. (2020) adopted a smaller area of 81 kpc^{-2} but excluded the diffuse emission toward the north and parts of tidal features that are included in our work. With their SFR estimate of 27.4 $M_\odot$ yr^{-1}, A. Adamo et al. (2020) assumed $\Sigma_{\rm SFR} = 0.34\ M_\odot$ yr^{-1} kpc^{-2}.

2.2. Optical Source Detection and Photometry

We use HST images taken in the near-UV (NUV; F275W), *U* (F336W), *B* (F438W), *V* (F555W), Hα (F665N), *I* (F814W), Paβ (F130N), and *H* (F160W) passbands. The observations used in this work are a mix of new WFC3 and archival Advanced Camera for Surveys (*B* and *I*) images, with the new data taken as part of the CCDG survey of extreme galaxies program (GO-15649; PI: Chandar) with the WFC3 camera.

Each individual exposure is processed though the standard Pyraf/STSDAS CALACS or CALWFC3 software before alignment and drizzling to a common grid using DRIZZLEPAC, creating a single, sky-subtracted image for each filter. Gaia DR2 sources (Gaia Collaboration et al. 2018) are used to astrometrically correct the *V*-band image, which is used as a reference for all other filters. FITS file outputs are in units of electrons per second and oriented with north up and east to the left.

For source detection, we use the DAOFIND detection algorithm in IRAF with a 3σ detection limit on the *V*-band image. At a distance of ∼69.7 Mpc, clusters in NGC 1614 appear as point-like sources in the HST data. In order to minimize effects from crowding and scatter in the measured colors, aperture photometry with a 2-pixel radius and background annuli between 7 and 9 pixels was performed on all sources in each filter. Background levels were determined as the median flux value after sigma clipping. Aperture corrections were determined from encircled energies derived from point sources in each filter, of 1.21 mag (F275W), 1.10 mag (F336W), 0.890 mag (F435W), 0.85 mag (F555W), 1.02 mag (F814W), and 0.76 mag (F665N). Magnitudes are converted to the VEGAmag system. We do not include background subtraction in the photometry performed on the non-continuum-subtracted Hα image, since the warm, ionized gas can have a different morphology than the starlight and is frequently in shells and rings around young clusters. We select clusters to have a measured *V*-band magnitude brighter than ∼26 mag to limit photometric errors, particularly in the bluer filters, and to have a concentration index (magnitude difference measured in apertures of 0.5 and 2 pixels) between 1.1 and 2.0 mag to eliminate extended background sources since clusters are expected to be point sources. Additional details on reduction and photometry are given in a paper presenting the CCDG survey (R. Chandar et al. 2024, in preparation).

A color image of NGC 1614 in the *B*, *V*, and Hα filters is shown in Figure 1. Three regions of interest are highlighted: the star-forming eastern arm, the dusty central region, and the dust- and Hα-free UV-bright arm. A 2-pixel radius (yellow circle) and annuli of 7 and 9 pixels (white circles) are shown on a cluster in the UV-bright arm as an example of the apertures used to perform photometry.

2.3. IR-only Detected Sources

Because NGC 1614 is an LIRG with significant amounts of dust, we use the Paβ and *H*-band infrared images to search for and estimate the number of optically obscured clusters. We do not, however, include Paβ or *H*-band measurements in our age-dating, due to the lower resolution of the IR camera compared with UVIS.

Using both the *H* band (F160W) and Paβ (F130N), along with a *V*-band image, we visually searched through the galaxy for any compact, point-like sources that appear in the two NIR filters but are not observed in the *V* band. Figure 2 shows an NIR *U*-, *I*-, and *H*-band color image of NGC 1614, with each of the clusters identified in the NIR circled in cyan. We identify 27 (∼2.4% of the sample) new sources in the *H*-band images that were not detected in *V* band, although all but 6 (∼0.5%) show at least some faint emission in the *I* band. All of the NIR sources are found in dusty areas, and a couple are found in somewhat isolated locations.

We will not include these 27 clusters in the rest of this work, as we are unable to age-date them. We are not able to determine whether these clusters are younger than 10 million years or not from the F130N Paβ filter, due to its poorer resolution and overlap with the *H* band in the bright and extended emission seen throughout these dusty regions, but we will present follow-up results from an accepted JWST proposal (GO-6035; PI: Caputo) in the future.

3. Cluster Analysis

In this section, we will estimate the age and mass for each cluster in our sample by comparing their measured magnitudes with predictions from stellar evolutionary models via SED fitting. One of the biggest challenges for these estimates lies in navigating the age–reddening degeneracy (e.g., B. C. Whitmore et al. 2023b). This is where older clusters—those that are intrinsically red with little to no extinction—have similar broadband colors to clusters that are moderately extinguished

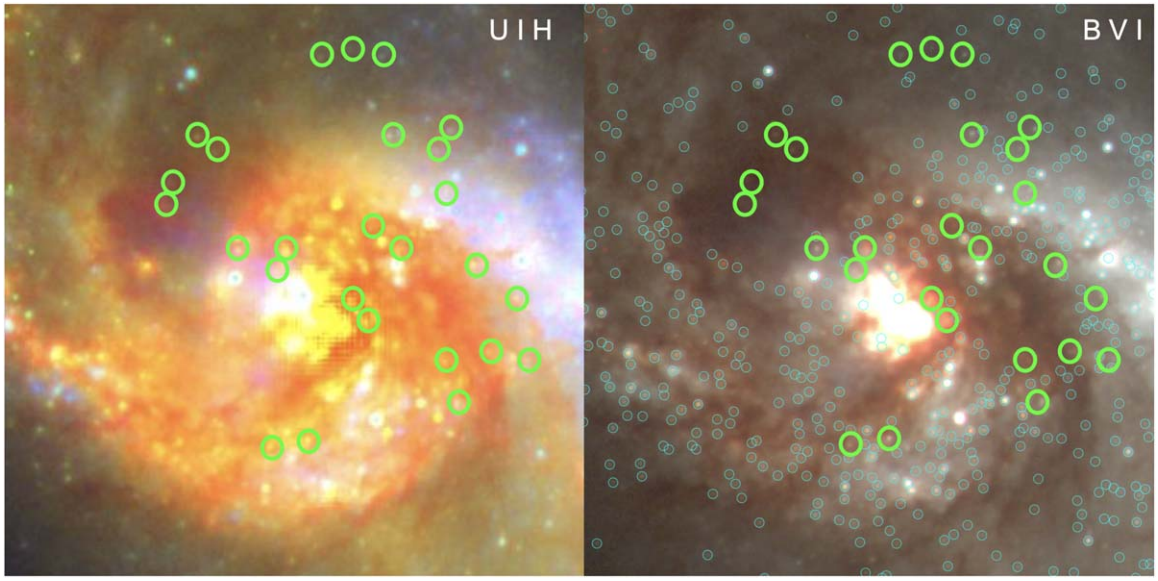

Figure 2. Left: *U*-, *I*-, and *H*-band HST color image of NGC 1614, with new sources visible in the NIR (*H* band) but not in the optical (*V* band) circled in lime green. These were identified by eye. Right: *B*, *V*, *I* HST color image with optically detected clusters circled in cyan and new NIR-only clusters circled in lime green.

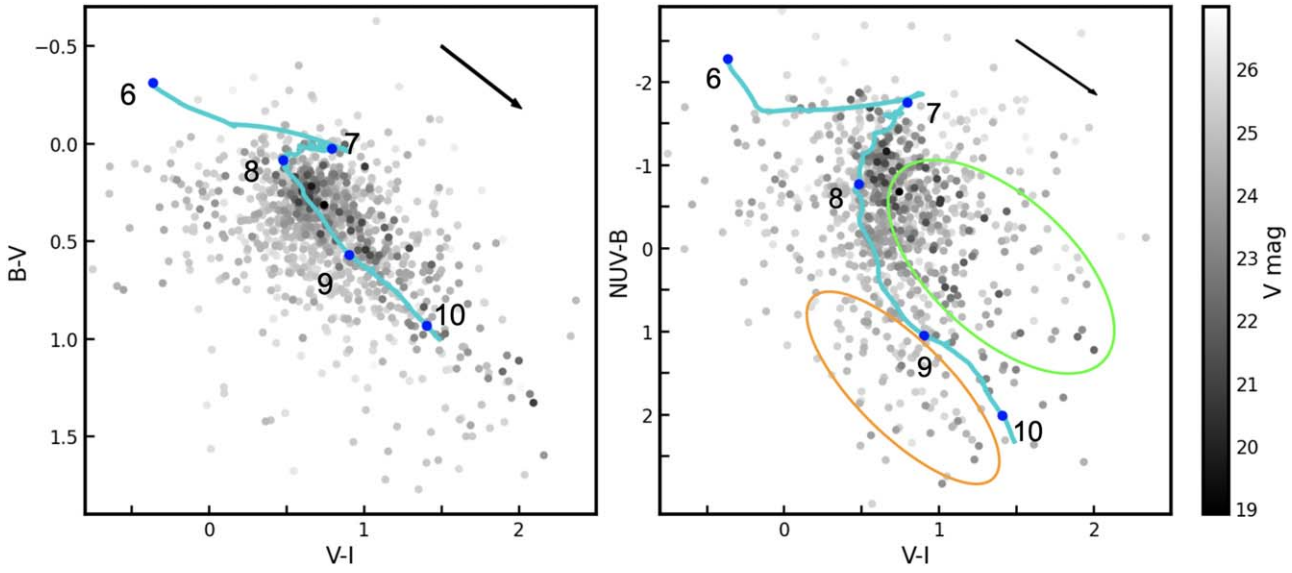

Figure 3. Color–color diagrams for clusters in NGC 1614 with $B-V$ vs. $V-I$ (left) and NUV – B vs. $V-I$ (right). The grayscale showing the *V*-band magnitude is to the right of the diagrams. Predictions from solar-metallicity (BC03) tracks (cyan) for cluster evolution are shown in blue for log (τ/yr) = 6, 7, 8, 9, and 10. A reddening vector with $A_V = 1.0$ is shown in the upper right corner of each panel.

and intermediate in age or, more likely, young and highly extinguished. We use two strategies to resolve the age–reddening degeneracy: (1) use available information to constrain the maximum $E(B-V)$ within subregions of the galaxy (see R. Chandar et al. 2023a), and (2) include Hα directly in the SED fits (B. C. Whitmore et al. 2010, 2020; R. Chandar et al. 2023a, 2023b).

3.1. Color–Color Diagrams and Training Sets

In Figure 3, we show color–color diagrams with measured magnitudes for the clusters in NGC 1614. These diagrams include predictions from solar metallicity (G. Bruzual & S. Charlot 2003, hereafter BC03) evolutionary models for cluster colors (plotted in cyan) from 1 Myr in the upper left to 10+ Gyr in the lower right, with each factor of 10 in age marked as blue circles. Clusters are plotted with colors that scale with their *V*-band magnitude, with the brightest clusters shown as the darkest points. The direction and amount that reddening will shift measured cluster colors by an $A_V = 1.0$ mag are represented by the arrow in the upper right corner of the color–color diagrams, assuming a Milky Way–like reddening law (E. L. Fitzpatrick 1999). Our cluster colors are not corrected for foreground extinction since it is fairly small (∼0.4 mag in *V* band; E. F. Schlafly & D. P. Finkbeiner 2011) compared with many clusters in this galaxy.

We find that the brightest clusters in NCG 1614 have a range in reddening. While many clusters closely follow the model track ($Av \lesssim 0.3$ mag), indicating that they experience little to no reddening in NGC 1614, a subset of bright clusters fall rightward of the model in the direction expected from reddening (Figure 3, circled in lime green). A visual

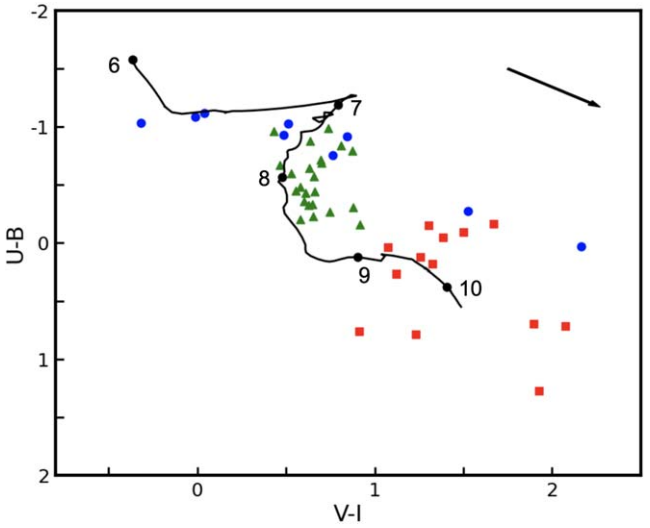

Figure 4. $U-B$ vs. $V-I$ color–color diagram with the BC03 model in black, Hα training set clusters shown as blue circles, UV-arm training set shown as green triangles, and old cluster training set shown as red squares. A reddening vector with an $A_V = 1.0$ is shown in the upper right corner.

examination of this subset shows that most have Hα emission and are therefore quite young ($\leqslant$6 Myr), recently formed clusters still (partially) embedded in and reddened by their natal gas and dust. There is another subset of clusters (circled in orange)—most clearly seen in the NUV – B versus $V-I$ colors—that fall below the models. These clusters are intermediate in age ($\approx$few $\times$ 100 Myr), with a range of reddening much like the Hα-emitting young clusters. A similar population of reddened, intermediate-age clusters exists in the dusty spiral galaxy NGC 1365 (B. C. Whitmore et al. 2023b).

To establish an appropriate maximum $E(B-V)$ to adopt during the SED fitting procedure (Section 3.3), we visually select the three training sets seen in Figure 4. These sets are composed of clusters with different ages, amounts of reddening, and magnitudes that are easily visually categorized into the following:

1. Very bright, young ($\leqslant$6 Myr) clusters, selected to have strong Hα emission and a range of broadband colors indicating different amounts of reddening.
2. Intermediate-age ($\approx$100 Myr) clusters in the nearly dust-free, western UV-bright arm with a range of V-band magnitudes.
3. Older clusters that appear red and show no obvious dust surrounding them in the images.

In Figure 4, young, strong Hα-emitting clusters (blue) have a large range of colors that fall off the models in the direction expected from reddening. We estimate the reddening of each cluster by comparing their measured colors with those predicted for a 3 Myr old cluster. We find that the maximum reddening experienced by clusters varies from one region to another within the galaxy. In the next subsection we will use properties of the Hα-emitting clusters as a prior to set the maximum $E(B-V)$ in different regions within NGC 1614.

The UV-bright arm provides an important, relatively dust-free laboratory to test parameters for our SED fitting. The clusters in this region follow the predicted model colors well (within $Av \sim 0.3$ mag), as seen by the green points in Figure 4, indicating that they all have similar intermediate ages (but a range of V magnitudes). Since there is essentially no Hα emission in this region, clusters in the western UV-bright arm to the west cannot be very young ($\tau \leqslant 6$ Myr) and reddened. This, paired with their locations on the color–color diagram and lack of dust in the region (see Figure 3), is strong evidence that their ages are on the order of $\approx$50–200 Myr. We find that restricting the maximum allowed $E(B-V)$ to low values (e.g., 0.1 mag) is important to correctly age-date these intermediate-age clusters.

Finally, a set of clusters that are very red ($B-V \geqslant 0.6$ and $V-I \geqslant 0.8$), bright (V-mag $\leqslant$ 24), and in relatively dust-free areas are identified and plotted in red in Figure 4. These clusters are expected to be older (log(age) $\geqslant$ 8.3), and we can restrict the maximum $E(B-V)$ to ensure that their estimated ages reflect this.

3.2. Constraints on Reddening by Region

NGC 1614 has a large range in reddening as seen by both visual inspection of the galaxy and the colors of young clusters. We develop a method to establish priors by determining the maximum $E(B-V)$ value to adopt in the SED fitting, which we allow to vary by region within the galaxy. Regions are determined by visual inspection and appear to have similar amounts of dust affecting the cluster colors. We want the maximum allowed $E(B-V)$ to be sufficiently high that reddened, young Hα-emitting clusters, which are younger than $\sim$6 Myr, are correctly age-dated, but not so high that older, gas-free clusters ($\geqslant$100 Myr) are erroneously fit by young ($\sim$10 Myr) ages and high reddening. In regions where the cluster colors hug the models closely and there is no indication of dust, low maximum $E(B-V)$ values are adopted.

NGC 1614 is segmented into regions, based on the color–color diagrams of Hα-emitting clusters, representing one of four maximum allowed $E(B-V)$ values: 0.1, 0.5, 1.0, and 2.0 mag.

Figure 5 shows the distribution of the clusters by reddening group on a color image to the right, with blue, green, orange, and magenta representing maximum $E(B-V)$ values of 0.1, 0.5, 1.0, and 2.0 mag, respectively. One subset of each of the four reddening groups is circled in the image to the right, as well as having their clusters represented in the $U-B$ versus $V-I$ color–color diagrams in the left panels, with the maximum $E(B-V)$ indicated. The progression in reddening is most obviously demonstrated by the young clusters with Hα emission, plotted in black, falling further off the models in the direction of the reddening arrow as one moves to dustier regions within the galaxy, as indicated by the increasing $E(B-V)_{\rm max}$ values.

The region shown with the lowest maximum $E(B-V)$ is the UV-bright arm, shown as the blue points in the top left panel of Figure 5. The cluster colors within this region are very close to the model track (within $Av \lesssim 0.3$ mag), with little evidence for reddening, and thus represent a relatively dust-free region. In addition, the clusters in this region should be older than 10 Myr, as there is no detected Hα emission and the colors suggest cluster ages closer to $\sim$100 Myr throughout the region. If we allow a maximum $E(B-V)$ of $>$0.1, age estimates for the clusters in this region start piling up around $\log(\tau/{\rm yr}) = 6.8$, an age where no H$\alpha$ emission is predicted, but which is erroneously young for these clusters. Restricting the maximum $E(B-V)$ to 0.1 for these relatively dust-free clusters allows for accurate age estimates. We therefore adopt a maximum E

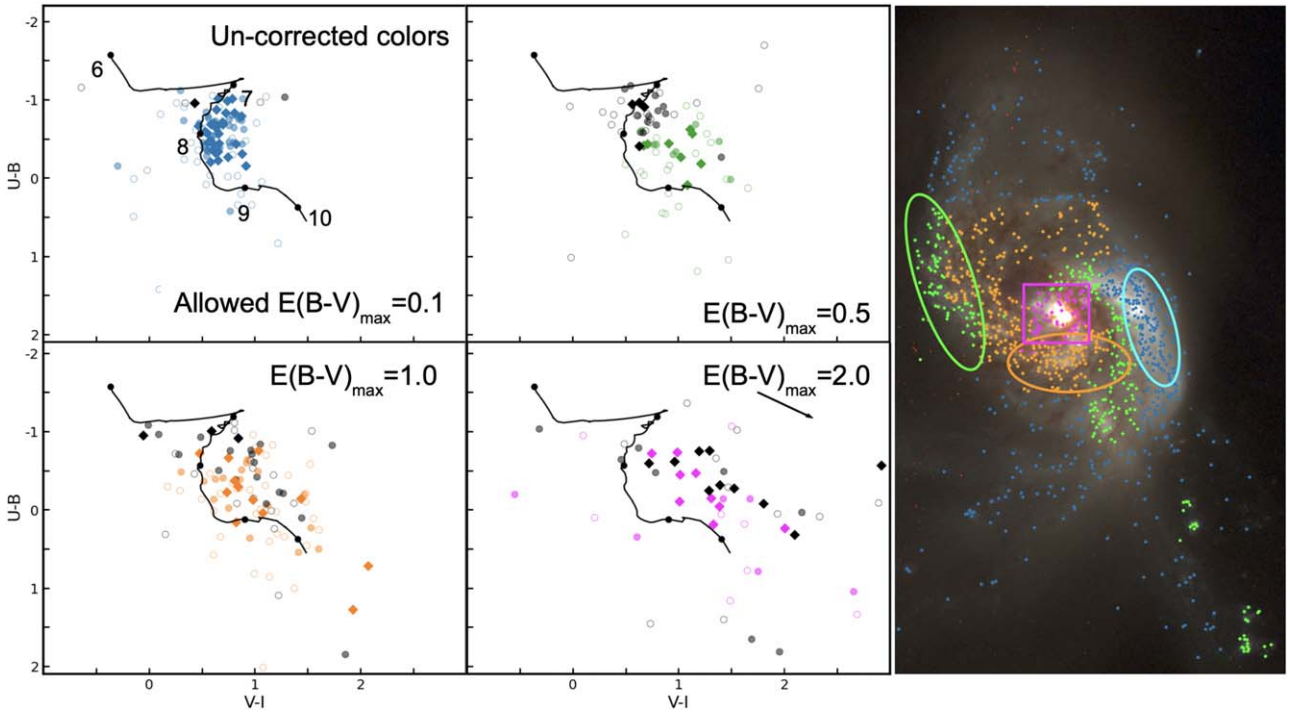

Figure 5. Right: *B*, *V*, *I* image of NGC 1614 with detected clusters overlaid; the color-coding shows the maximum $E(B-V)$ allowed during the age-dating fits. Left: uncorrected $U-B$ vs. $V-I$ color–color diagrams of four example regions with assigned maximum allowed $E(B-V)$ of 0.1 mag (top left), 0.5 mag (top right), 1.0 mag (bottom left), and 2.0 mag (bottom right). A reddening vector of $A_V = 1.0$ is shown in the bottom right image. Diamonds indicate clusters with *V*-mag ≤ 23.5, filled circles represent $23.5 <= V\text{-mag} < 24.5$, and open circles represent *V*-mag ≥ 24.5. Data points outlined and filled in black indicate that the cluster has Hα emission and is younger than ≈6 Myr. These regions illustrate the different amounts of reddening due to dust found for clusters in different regions within NGC 1614.

$(B-V) = 0.1$ mag during SED fitting for clusters in the UV-bright arm and others shown in blue across the galaxy.

A portion of the eastern, star-forming arm is shown in green and represents regions with modest reddening. Clusters in this region begin to fall farther to the right of the models than seen in regions like the UV-bright arm. There are a number of somewhat reddened Hα-emitting clusters to the right of the model. These clusters need a somewhat higher $E(B-V)$ in order to be correctly fit to a young age, but they do not require more than $E(B-V) = 0.5$ mag.

The region to the south of the center of NGC 1614, plotted in the bottom left panel in orange, illustrates a moderately dusty region in the galaxy. Hα-emitting clusters have colors that fall further still along the reddening vector, with some having colors similar to those expected for ancient globular clusters. Note, however, that we expect to detect very few globular clusters at the distance of NGC 1614. This region is given a maximum $E(B-V) = 1.0$ mag to allow the Hα-emitting clusters to be fit by a young age.

Finally, the central region of NGC 1614, plotted in magenta, is given the largest maximum $E(B-V) = 2.0$ mag because of the large amount of dust and highly reddened young clusters in this region, a few of which required an $E(B-V) \geqslant 1.5$ to be correctly age-dated. Hardly any clusters in this region fall on the BC03 model. This is also the only region in NGC 1614 given a maximum $E(B-V) > 1.0$ mag. Comparing results for this region when we adopt a maximum $E(B-V)$ of 1.5 mag versus 2.0 mag, only a few clusters, confirmed by eye to have Hα emission, correctly move to ages less than 6 Myr with a maximum $E(B-V)$ of 2.0 mag. All other clusters have the same best-fit ages in both cases.

A total of 525 clusters (46.4% of the total sample) are given the lowest maximum $E(B-V)$ value of 0.1 mag. These clusters show little to no deviation from the models in color–color space and no indication of dust from visual inspection, similar to the blue UV-bright clusters in Figure 5. There are 247 clusters (21.8%) that are allowed a slightly higher level of reddening with a maximum $E(B-V) = 0.5$ mag. Clusters in these areas of the galaxy show small deviations from the models in the direction of reddening, and a visual inspection shows low amounts of dust (green clusters in Figure 5). There are 301 clusters (26.6%) that have a maximum adopted $E(B-V)$ value of 1.0 mag. There is a noticeable amount of dust in these areas of the galaxy, leading to clusters falling to the right of the models (orange clusters in Figure 5). Finally, one region composed of 59 clusters (5.2%) is given the highest maximum value of $E(B-V) = 2.0$ mag during SED fitting. This region is in the center of the galaxy and has a noticeably higher amount of dust than the other regions, seen in magenta in Figure 5.

3.3. Age-dating: Method, Results, and Checks

We estimate the age, reddening, and mass of clusters in NGC 1614 by comparing the measured luminosities over six HST bands (NUV, *U*, *B*, *V*, Hα, and *I*) to predictions from the solar-metallicity BC03 model with the maximum $E(B-V)$ values described in Section 3.2. The *H*-band and Paβ filters are not used in the fit, due to their poorer resolution and photometry. NGC 1614 has a value of 12 + log (O/H) = 8.69, consistent with solar metallicity (C. W. Engelbracht et al. 2008; M. Modjaz et al. 2011). Although any globular clusters will likely have subsolar metallicity, we expect to detect very few of these ancient clusters at a distance of

~70 Mpc. We also restrict our analysis in Section 4 to clusters younger than 0.5 Gyr, which are sufficiently young that we expect them to have approximately solar metallicity.

We use the BC03 models for age-dating. While there are newer models that incorporate improved prescriptions for mass loss (e.g., C. Maraston 2005) and other models that include binaries and binary evolution (e.g., J. J. Eldridge & E. R. Stanway 2009; E. Zackrisson et al. 2011), we find that the BC03 models predict cluster colors that provide a better overall match to the observed colors of clusters. For example, the PHANGS-HST collaboration found that the colors of ~100,000 star clusters and associations in nearby spiral galaxies are well fit by the BC03 models. In particular, D. Maschmann et al. (2024) show that the measured $(V-I)$ colors of clusters do not extend redward of the BC03 model predictions at 10 Myr. However, a number of newer population synthesis models predict redder $(V-I)$ colors than are observed (e.g., C. Maraston 2005; E. Zackrisson et al. 2011).

In addition to photometry in broadband filters, we directly include photometry measured in the F665N narrowband filter (which is not continuum subtracted) in our fits. To predict the strength of Hα, we use the number of ionizing photons predicted by the BC03 models and assume case B recombination to calculate the recombination line flux. The predicted line emission is added to the stellar continuum at a given age in order to model the narrowband filter. Our default age-dating assumes that no ionizing photons escape ($f_{\rm esc} = 0.0$), but we find that there is little impact on the age estimates if we assume $f_{\rm esc} = 0.5$ instead.

Hα emission is very strong for the youngest clusters and falls off quickly as they age. The exact timescale for Hα emission to essentially disappear is model dependent. The BC03 models predict that this line emission is essentially gone by 6 Myr. This is similar to predictions from Starburst99 (C. Leitherer et al. 1999). Models that include binaries like BPASS (J. J. Eldridge & E. R. Stanway 2009) can extend the life of Hα emission to ~10 Myr when Wolf–Rayet stars are included, but this emission still peaks at ages of $\lesssim$4 Myr without them (T. Z. Dorn-Wallenstein & E. M. Levesque 2018).

The grid for the SED fit runs over ages of $\log(\tau/{\rm yr}) = 6.0$–$10.2$ and reddening $E(B-V) = 0$ to the allowed regional maximum (0.1, 0.5, 1.0, or 2.0 mag). The best-fit values for age and reddening for each cluster are found through minimizing the statistic: $\chi^2(\tau, A_V) = \sum_\lambda W_\lambda (m_\lambda^{\rm obs} - m_\lambda^{\rm mod})^2$, where $m^{\rm obs}$ and $m^{\rm mod}$ are the observed and model magnitudes, respectively. Masses for each cluster are estimated from the extinction-corrected V-band luminosity, the age-dependent mass-to-light ratios predicted by the models, and the assumption that the distance modulus is 34.2 mag. We compute the 1σ error for each cluster from the χ^2 statistic. We show the median uncertainty for clusters in the 1–10 Myr, 10–100 Myr, and 100–400 Myr age intervals at the top of Figure 7. These range from ~0.15 to 0.2 in $\log\tau$, with the youngest and oldest age intervals having median 1σ errors of ≈0.2 and the middle interval having somewhat smaller median errors of ≈0.15.

Stochasticity is not expected to have much impact on cluster colors and hence on age and mass estimates, since the majority of clusters in NGC 1614 are quite massive with $M > 10^5\,M_\odot$. Stochastic fluctuations start to have a small effect on clusters with masses $\sim 3\times10^4\,M_\odot$ (P. Goudfrooij & R. S. Asa'd 2021) and become more pronounced at masses below $\sim 5\times10^3\,M_\odot$ in the blue and optical regimes we are probing here (M. Fouesneau et al. 2012).

Figure 6 shows $U-B$ versus $V-I$ color–color diagrams for the same four regions as Figure 5, but with cluster colors corrected by their best-fit $E(B-V)$ values after age-dating. For all regions, the Hα-bright clusters, shown in black, have moved to the upper left of the models, where young clusters are expected to be. In the regions with larger $E(B-V)_{\rm max}$ values, clusters without Hα stay along the older portion of the model track and do not move to young ages.

Ages of the bright clusters in the UV-bright arm, shown in blue in Figure 6, have estimated ages between ~25 and 250 Myr. However, if we allow the maximum $E(B-V)$ to increase to 0.5 during age-dating for clusters in this region, the majority are best fit by too young of an age (~6–10 Myr) and too-high reddening. The direct inclusion of Hα in the fits prevents these (and other) clusters with no Hα emission from being age-dated to less than ~6 Myr, where the models predict that the Hα luminosity plummets. However, it does not prevent them from having estimated ages between 7 and 10 Myr, which is why limiting the maximum $E(B-V)$ is important.

We compare our final age estimates with the results when assuming a single value of $E(B-V)_{\rm max} = 1.5$ mag for the entire cluster population during age-dating, since this has been the default assumption for many studies (e.g., D. Calzetti et al. 2015; A. Adamo et al. 2020; J. C. Lee et al. 2022). Not surprisingly, many clusters that were initially best fit by ages older than $\log(\tau/{\rm yr}) > 7.5$ using our variable maximum $E(B-V)$ method have estimated ages younger than $\log(\tau/{\rm yr}) < 7.0$ when a higher maximum $E(B-V)$ is allowed. The vast majority (~90%) of these clusters are fainter than $m_V = 24$ mag, and none have associated Hα emission. The clusters that change age estimates are found throughout the galaxy but are concentrated in areas with little ongoing star formation and dust, like the UV-bright arm and tidal tails. Therefore, we find that adopting a single value of $E(B-V)_{\rm max} = 1.5$ mag results in incorrect (too-young) age estimates for many clusters. This issue has been pointed out in other recent studies as well. Approximately 80% of old globular clusters in the PHANGS-HST survey of nearby spiral galaxies were best fit by ages that were too young by factors of 10–1000 (B. C. Whitmore et al. 2023a; M. Floyd et al. 2024). A number of intermediate-age clusters were also best fit to ages <10 Myr .

4. Results for Clusters

4.1. Age–Mass Diagram

In Figure 7, we present the final age–mass diagram for clusters in NGC 1614. Clusters range in age from $\log(\tau/{\rm yr}) \approx 6$ to 10.3 (~1 Myr to >10 Gyr) and have estimated masses between $\sim10^4$ and $2\times10^7\,M_\odot$. The magnitude limit of our observations is $M_V = -8$ mag and shown as the dashed black line along the bottom edge of the age–mass diagram, where we have assumed a distance modulus of 34.2 mag. Above the luminosity limit of the sample, there are more lower-mass clusters ($M \lesssim 10^5\,M_\odot$) than high-mass ones at any given age. The luminosity limit also restricts us to higher-mass clusters at older ages because they fade over time.

The gap observed in cluster ages between $\log(\tau/{\rm yr}) \sim 7.0$ and 7.5 is due to well-understood biases from the age-dating process where the models loop back on themselves, and it does not indicate an actual gap in cluster formation

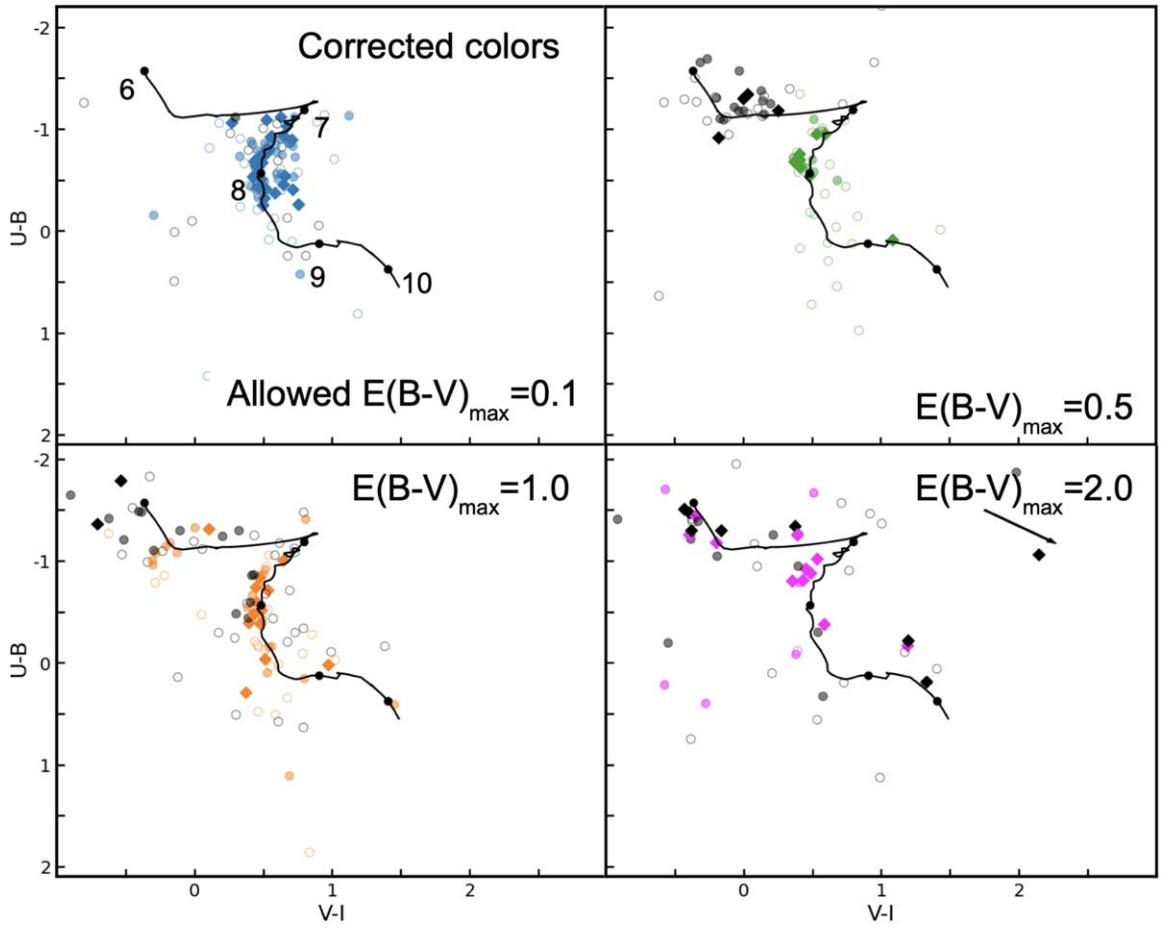

Figure 6. Same as the left panel of Figure 5, but with cluster colors corrected for best-fit values from age-dating.

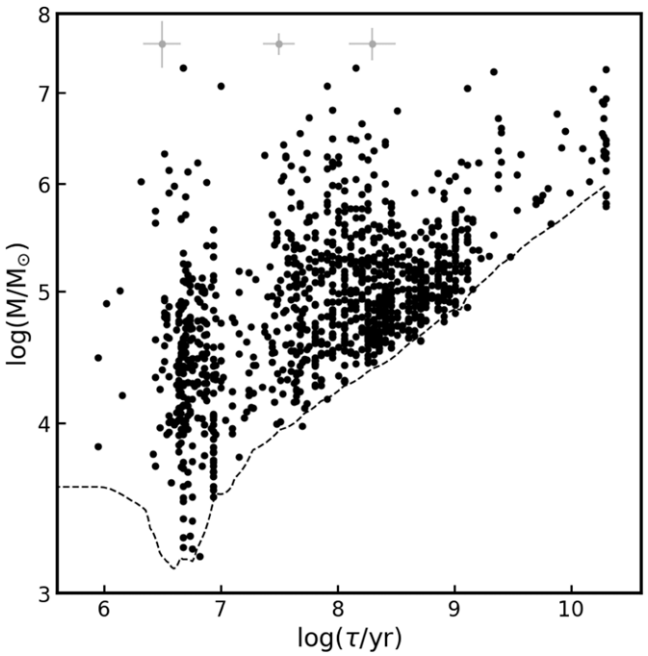

Figure 7. Cluster age–mass diagram for NGC 1614. The dashed line represents $M_V = -8$ mag, the approximate completeness limit for individual clusters in our sample. Median error bars are plotted for clusters above the completeness limits for the 1–10 Myr, 10–100 Myr, and 100–400 Myr age intervals (see text).

(M. Gieles et al. 2005; R. Chandar et al. 2010; Q. E. Goddard et al. 2010). There is a distinct lack of clusters younger than $\lesssim$3 Myr. This is likely a bias in our age-dating procedure, where it is hard to differentiate the ages of clusters between 1 and 4 Myr, often due to the amount of reddening that affects their broadband colors. However, this bias should have little impact on the results of this paper. We bin all clusters from 1 to 10 Myr into a single interval for our analysis of the CMF and Γ. Smaller bins are used in the age distribution, but the gaps are factored into the bins used there as well. We do not use clusters older than $\log(\tau/\mathrm{yr}) = 8.6$ ($\sim$400 Myr) in our analysis since at least some of these can be affected by the age–metallicity degeneracy (e.g., R. Chandar et al. 2004; D. A. Forbes et al. 2022; B. C. Whitmore et al. 2023a). We restrict the rest of our analysis to clusters younger than log $\log(\tau/\mathrm{yr}) = 8.6$ and brighter than $M_V = -8$ mag.

4.2. Mass Function

The shape of the CMF—and how it changes over time—can give critical insight into the formation and dissolution of clusters in a galaxy, for example, if there is a physical upper limit to the masses of clusters or whether mass-dependent or mass-independent disruption dominates cluster demographics. The mass function of very young clusters with ages $<$10 Myr approximately represents the "initial" CMF (ICMF). A comparison of the shape and normalization of this distribution

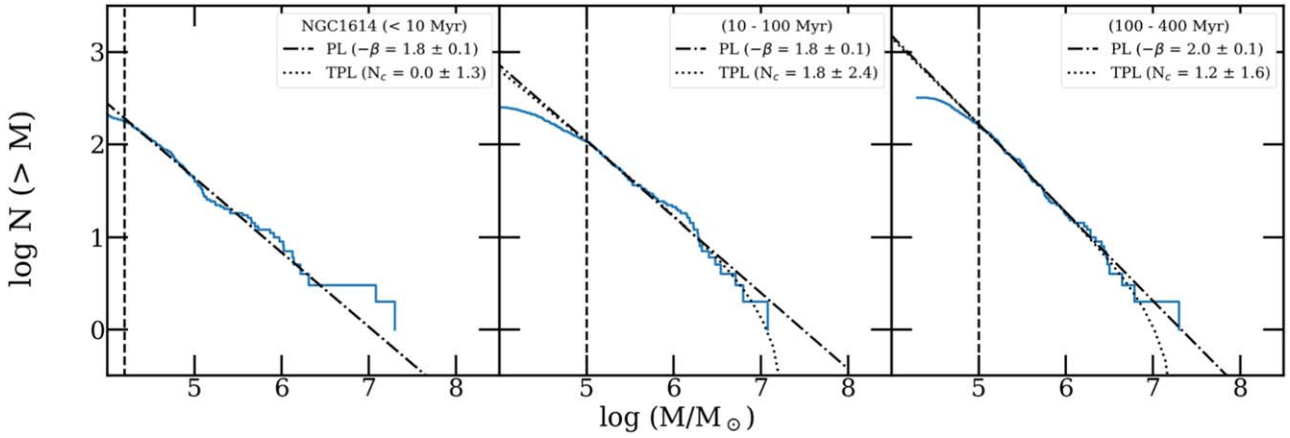

Figure 8. Cumulative mass functions for clusters in NGC 1614 in age intervals of 1–10 Myr, 10–100 Myr, and 100–400 Myr. The adopted completeness limit, where each distribution flattens from a power law, is shown as the dashed vertical line. Fits to a power-law fit are shown as the dotted–dashed lines, and fits to a truncated power law are shown as the dotted line. The best-fit values of β for a power law (PL) and the statistic N_C, which represents the upper end of a truncated power law (TPL), are given in the upper right corner of each panel. See text for details.

with that of older clusters is important for understanding their evolution.

We study the CMF in three different age intervals, 1–10 Myr, 10–100 Myr, and 100–400 Myr. Figure 8 shows the cumulative CMF in each of the three age intervals. For each one, the distribution increases in an approximately power-law fashion before flattening toward the lower-mass end. The flattening at the lower-mass end of the CMF is assumed to be due to sample incompleteness, not to a physical effect. We determine the completeness limit for each distribution as the mass where the distribution deviates below a power law at the 99% level (dashed vertical line). The completeness limits are found to be $\log(M/M_{\odot}) = 4.2$ (<10 Myr), 5.0 (10–100 Myr), and 5.0 (100–400 Myr).

The best-fit single power law with $dN/dM \propto M^{\beta}$ down to the completeness limit is shown as the dotted–dashed line in each panel. These fits give $\beta = -1.8$, -1.8, and -2.0 ± 0.1 for 1–10 Myr, 10–100 Myr, and 100–400 Myr respectively. This means that the CMFs can be described by a single power law with index $\beta = -1.9 \pm 0.1$ for NGC 1614, and there is no obvious evolution in the shape of the mass function over the first ≈0.5 Gyr.

Some previous works have found that CMFs are significantly better described by a Schechter function than by a single power law (N. Bastian et al. 2012; L. C. Johnson et al. 2017). A Schechter function has the form $\psi(M) = dN/dM \propto M^{\beta} \exp(-M/M_{\star})$, a power law with an index β with an exponential cutoff at a value $M_{\star}$ at the upper end. To test for a potential upper cutoff in the mass function, we use the maximum likelihood method developed and described in A. Mok et al. (2019). This method uses all clusters above the completeness limit and does not bin the clusters or use a cumulative distribution to smooth over any features. The best fit for these parameters, shown by the dashed lines, is obtained by maximizing the likelihood function. The 1σ, 2σ, and 3σ confidence contours can be defined in the β–M_{*} plane using the formula $\ln(L) = \ln(L_{\max}) - 1/2\chi_p^2(k)$, where p is the confidence level and k is equal to the number of free parameters in the fit.

The results for our maximum likelihood fits to a Schechter function are plotted in Figure 9 for each age range. These plots show the 1σ, 2σ, and 3σ confidence intervals (black, gray, and light gray, respectively) for the maximum likelihood fit of the power-law index $-\beta$ and the cutoff mass $\log(M_{\star}/M_{\odot})$. The most massive cluster observed in each age interval is plotted as a green triangle. A wide range of $M_{\star}$ values is allowed by each distribution, because the 2σ and 3σ confidence contours start near $10^{6.5}\,M_{\odot}$ and continue without closing to the right edge of the diagrams at $10^{8.5}\,M_{\odot}$ for all three intervals, and even the 1σ contour is open all the way to the edge for 1–10 Myr clusters. This means that the CMFs are consistent with being drawn from a pure power law rather than requiring a Schechter-like cutoff at the upper end.

We note that uncertainties for the mass estimates were not included in the maximum likelihood fits. Including uncertainties in the fits would further broaden the contours, making any detection of $M_{\star}$ even less significant.

As an independent check on the results from the maximum likelihood method, we also fit a broken power law to the cumulative mass distributions in Figure 8. A broken power law allows a more gradual downturn than an exponential and acts like a simplified Schechter function. This is described by $N(M' > M) = N_c\,[(M/M_{\star})^{\beta+1} - 1]$, where N_c must be statistically significant ($\geqslant 3\sigma$) to indicate that a truncation better represents the upper end of the distribution than a single power law. The best truncated power-law fits to the CMFs are shown as the dotted lines in Figure 8. None of the N_c values reach 3σ, indicating that a truncated power law is also not a good fit to the CMFs in NGC 1614 in any of the age intervals studied here.

At the distance of ∼70 Mpc, it is possible that multiple clusters could blend together and appear as a single, massive cluster instead. Z. Randriamanakoto et al. (2013) experimented on the nearby (∼20 Mpc) merging Antennae galaxies to test the effects of blending on super star clusters. They degraded HST images to mimic how the Antennae would look at a distance of 70 Mpc, nearly the exact same distance as NGC 1614. They found that while blending can flatten the observed cluster luminosity function, the effect is minor and barely detectable outside of the fit uncertainties. We have run a few experiments along the lines of those performed in Z. Randriamanakoto et al. (2013) and R. Chandar et al. (2023b) to see whether blending has a strong impact on our results. These experiments include (1) splitting the most massive cluster in each age bin into three equal-mass ones, (2) taking 10 random clusters from the 50 most massive and splitting them into three equal-mass clusters, and (3) deleting them from the catalog. The mass functions for

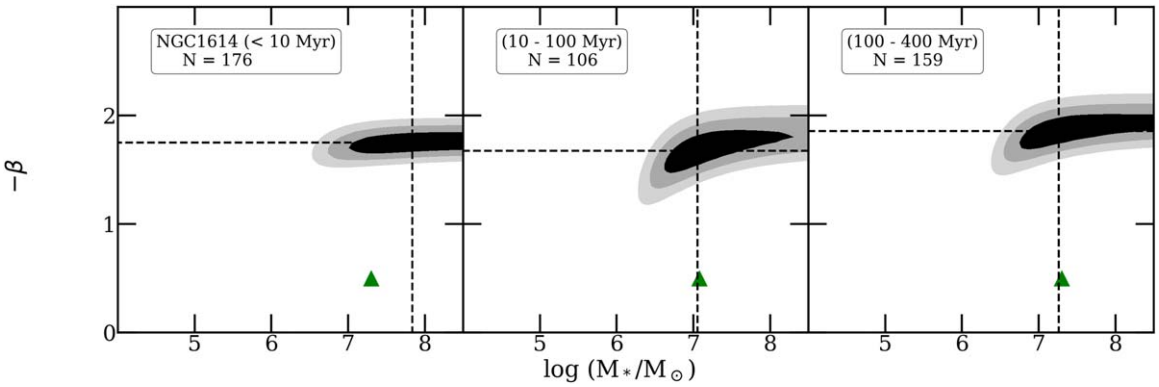

Figure 9. Maximum likelihood fit results to the power-law index β and upper mass cutoff M_* are shown for <10 Myr, 10–100 Myr, and 100–400 Myr clusters. The most massive cluster in each age range is plotted as the green triangle. The most likely $-\beta$ and M_* values are shown as the horizontal and vertical dashed lines, respectively. The 1σ (black), 2σ (gray), and 3σ (light gray) confidence intervals are also shown. There is no convergence for M_* in any age range, indicating that the data do not prefer an exponential upper mass cutoff.

all of these experiments have best-fit values of the power-law index β that are within the errors of our initial fit, and none show any indication of a Schechter-like cutoff.

For NGC 1614, we find no significant detection of an upper mass cutoff in the CMFs, and we find that the shape of the CMF does not evolve over the first ≈0.5 Gyr over the plotted range of masses.

4.3. Age Distribution

Cluster age distributions encode important information on the formation and disruption histories of the clusters. Cluster age distributions for NGC 1614 are plotted in Figure 10 for three mass intervals: $\log(M/M_\odot) \geqslant 5.8$, $\log(M/M_\odot) = 5.8$–5.4, and $\log(M/M_\odot) = 5.0$–5.4. All of these clusters have luminosities that are above the completeness limit. These are plotted as the number of clusters within the age bin versus the amount of time covered by the bin. We have used fairly broad bins in log (τ) to smooth out the small-scale features and age-dating artifacts seen in the age–mass diagram (Figure 7).

We model each age distribution as a power law, $dN/d\tau \propto \tau^{\gamma}$, and fit for the power-law index γ. Horizontal bars are the width of the age bin, and vertical error bars are calculated from Poisson statistics. We find that the age distributions for all three mass intervals decline continuously starting at young ages and are similar within the uncertainties. This means that the age distributions are independent of their masses, at least in the mass ranges probed here. We find that a power-law index of $\gamma \approx -0.5 \pm 0.1$ describes the cluster age distributions in NGC 1614.

We expect that there are at least some very young, recently formed clusters that remain obscured at optical wavelengths but that can be detected by high-resolution imaging in the infrared with JWST, similar to the clusters identified in Section 2.3. This population of young, embedded clusters might further steepen the power-law index for the cluster age distribution if they were included, an effect that was observed recently by S. T. Linden et al. (2023) for the dusty, merging system VV 114. This very young, optically obscured cluster population will be explored using upcoming JWST observations.

4.4. Fraction of Stars in Clusters

The fraction of stars that are born in clusters, also known as the cluster formation efficiency (Γ), is a fundamental property

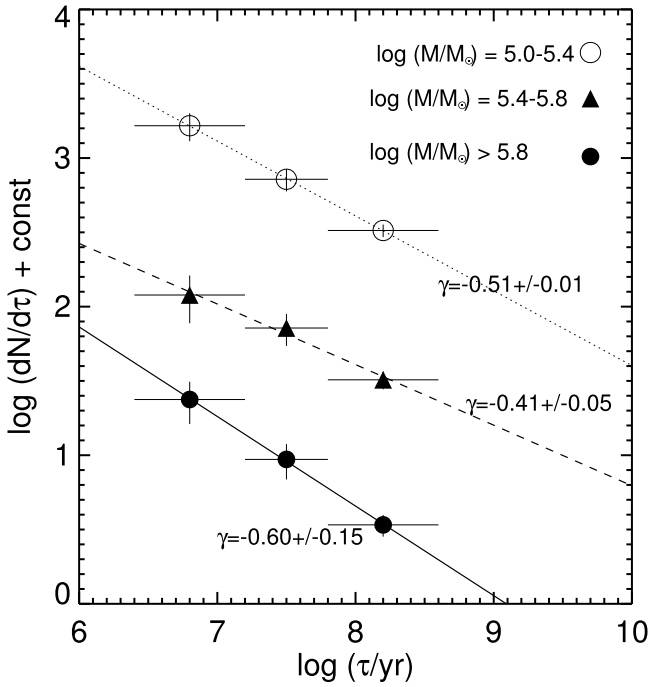

Figure 10. Age distributions of star clusters in NGC 1614 in the three indicated mass intervals. Fitted lines show power laws, $dN/d\tau \propto \tau^{\gamma}$, with the best-fit value of γ indicated.

of star and cluster formation on galaxy scales. Simulations mostly find that Γ increases significantly with $\Sigma_{\rm SFR}$. Typically, Γ is calculated from the stellar mass found in very young (1–10 Myr) clusters, which we refer to as $\Gamma_{1-10\,\rm Myr}$. Fewer works have estimated the fraction of stars that remain in clusters at older ages. In this section, we calculate the fraction of stars found in clusters within NGC 1614 as an additional data point at the high end of SFR and $\Sigma_{\rm SFR}$. We track this fraction from very young (1–10 Myr) clusters to those in older (10–100 Myr and 100–400 Myr) clusters.

In order to calculate the fraction of stars in clusters in any age interval, we must calculate both the total mass of stars born during that time interval and that found within the compact cluster population. We summarize our method below, which follows standard practices developed initially in Q. E. Goddard et al. (2010) and used in a number of recent works

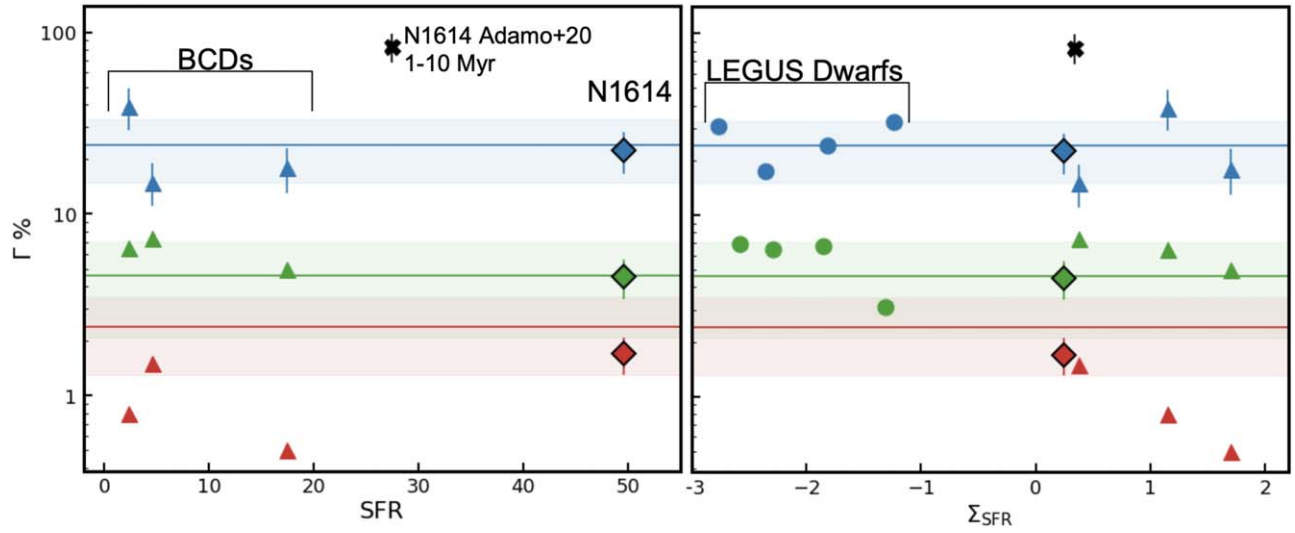

Figure 11. Comparison of Γ values of different galaxies and age intervals. Γ_{1-10} is plotted in blue, Γ_{10-100} in green, and $\Gamma_{100-400}$ in red. Values for NGC 1614 in this work are plotted as diamonds, and Γ_{1-10} for NGC 1614 from A. Adamo et al. (2020) are plotted as black crosses. Blue compact dwarf galaxies from R. Chandar et al. (2023b) are plotted as triangles. Binned dwarfs in the LEGUS from D. O. Cook et al. (2023) are plotted as circles. The relationships found in R. Chandar et al. (2017) are the lines with shaded error regions in each color.

(e.g., A. Adamo et al. 2015, 2020; R. Chandar et al. 2017; D. O. Cook et al. 2023).

To find the total mass of stars in clusters, we first sum up the masses of all observed clusters above the completeness limit of our sample (see Section 4.2 and Figure 8). The total stellar mass in clusters below the completeness limit is determined by extrapolating the CMF from the completeness limit down to $100\,M_\odot$ assuming a power law with an index of -2.0. This power-law index is similar to the best fits we determined for the CMFs in NGC 1614 (see Section 4.2). The power law is integrated and added to the mass in clusters above the completeness limit to get the total mass of stars in clusters.

The total mass of stars in the galaxy is found by multiplying the total SFR of the galaxy by the time elapsed in the age interval. Γ is then simply the ratio of the mass of stars in clusters divided by the total stellar mass. For our calculations, we adopt an SFR of $49.6\,M_\odot\,\mathrm{yr}^{-1}$ (C. Giménez-Arteaga et al. 2022) for NGC 1614 (see Section 2.1) with an uncertainty of ∼25% (following D. O. Cook et al. 2023 and R. Chandar et al. 2023b).

We calculate the fraction of stars that are born in clusters to be $\Gamma_{1-10\,\mathrm{Myr}} = 22.4\% \pm 5.7\%$. We find the fraction of stars that remain in the 10–100 Myr and 100–400 Myr age intervals to be $\Gamma_{10-100} = 4.5\% \pm 1.1\%$ and $\Gamma_{100-400} = 1.7\% \pm 0.4\%$.

5. Discussion

5.1. No Cutoff in the Cluster Mass Function

The observed CMF can be used to infer maximum cluster masses and other properties such as Γ. It has been suggested that the CMFs of galaxies have a similar power-law index of $\beta = -2$ (e.g., Q. Zhang & S. M. Fall 1999; S. M. Fall & R. Chandar 2012; R. Chandar et al. 2017; H. Li et al. 2017, 2018; M. R. Krumholz et al. 2019; M. Y. Grudić et al. 2021), but with high-mass cutoffs (M_*) that increase with Σ_{SFR} (L. C. Johnson et al. 2017). Recent simulations both re-create and utilize the physics driving the CMF. Tests constraining the ICMF include magnetohydrodynamical simulations of turbulent, star-forming giant molecular clouds (GMCs; M. Y. Grudić et al. 2021, 2023), while cosmological simulations have included star clusters as a unit of star formation in high-redshift Milky Way–sized galaxies (H. Li et al. 2017, 2018).

With the adopted SFR for NGC 1614 from C. Giménez-Arteaga et al. (2022) of $49.6\,M_\odot\,\mathrm{yr}^{-1}$, we can use the relationships from the fiducial run in H. Li et al. (2017) of $M_* \approx 1.4 \times 10^4\,M_\odot \times \mathrm{SFR}^{1.6}$ and $M_{\mathrm{max}} \approx 8.8 \times 10^4\,M_\odot \times \mathrm{SFR}^{1.4}$ to calculate the most massive cluster (M_{max}) and M_* predicted in NGC 1614. M_*, according to the relation, is calculated to be $7.2 \times 10^6\,M_\odot$ and M_{max} to be $2.1 \times 10^7\,M_\odot$ for a galaxy with the SFR of NGC 1614.

The most massive cluster observed in NGC 1614 is $2.0 \times 10^7\,M_\odot$, which agrees well with the predicted value from H. Li et al. (2017). However, as presented in Section 4.2, no high-mass cutoff is found in the CMF in this galaxy. Therefore, our results do not agree with the predicted cutoff value of $7.2 \times 10^6\,M_\odot$ from H. Li et al. (2017).

As our results only probe ∼3% of the Hubble time, it is reasonable to assume that the physics of cluster formation has not changed significantly over the past 400 Myr.

5.2. Constraints on Cluster Formation and Disruption

The study of cluster formation is entwined with cluster disruption. Based on global estimates of the SFR from tracers that are sensitive to different age intervals, we concluded that the star formation history of NGC 1614 has likely been fairly constant (within a factor of ≈2–3) for the past ∼0.5 Gyr (see Section 2.1). A fairly constant star formation history is also supported by the continuous distribution of cluster colors along the cluster evolutionary track (Figure 3), which does not show gaps or concentrations in any particular age interval. These distributions contrast with the color distributions and age–mass diagrams for a post-starburst galaxy like S12 (R. Chandar et al. 2021) and NGC 34, which is an LIRG that is post-merger and appears to be post-burst (Y. Zhang et al. 2024, in preparation). All of these points support our assumption that NGC 1614 has been forming stars and clusters at a fairly constant rate.

5.2.1. Cluster Formation

Γ_{1-10} is a tracer of the cluster formation efficiency and measures the percentage of stars that are born in clusters. In NGC 1614, an extreme system with a high SFR, Γ_{1-10} can tell us about galactic-scale star formation and whether cluster formation is more efficient in more extreme systems.

Simulations of Γ_{1-10} over the past decade vary in approach and assumptions, but all predict an increase in Γ_{1-10} with $\Sigma_{\rm SFR}$. These simulations range from analytical scaling predictions (J. M. D. Kruijssen 2012) to magnetohydrodynamical simulations of GMCs and model cluster populations. Different prescriptions for feedback can dramatically impact the Γ–$\Sigma_{\rm SFR}$ relation (e.g., H. Li et al. 2018; F. Dinnbier et al. 2022; M. Y. Grudić et al. 2022). The predicted increase over a factor of $\sim10^4$ in $\Sigma_{\rm SFR}$ ranges from a factor of $\sim100\times$ (J. M. D. Kruijssen 2012) to only ~2 (F. Dinnbier et al. 2022). For a system like NGC 1614, the simulations predict a Γ_{1-10} between 3% and 60%, with most predictions in the 20%–50% range. This large range in predicted values underscores the importance of empirical estimates of Γ_{1-10} in galaxies with high $\Sigma_{\rm SFR}$.

We calculate the fraction of stars that form in clusters to be $\Gamma_{1-10\,\rm Myr} = 22.6\% \pm 5.7\%$. This fraction may be somewhat higher if there is a significant number of massive, deeply embedded young clusters, but our NIR images (Section 2.3) tentatively indicate that optically obscured clusters are likely to have lower masses and hence not to have a significant impact on Γ_{1-10}. Our $\Gamma_{1-10\,\rm Myr}$ of $22.6\% \pm 5.7\%$ agrees well with the range of $\Gamma_{1-10} = 24\% \pm 9\%$ found in eight galaxies that range from dwarfs to spirals to mergers (R. Chandar et al. 2017), as seen in Figure 11. It is similar to the results found for 23 nearby dwarf and irregular galaxies studied as part of the Legacy ExtraGalactic UV Survey (LEGUS) of $\Gamma_{1-10} = 27\,\% \pm 6\%$ (D. O. Cook et al. 2023). This value is also similar to that found for three blue compact dwarf galaxies from the CCDG sample, dwarf galaxies with some of the highest $\Sigma_{\rm SFR}$ in the nearby universe (R. Chandar et al. 2023b).

On the other hand, some previous works have found significantly higher values for Γ_{1-10} for galaxies with high $\Sigma_{\rm SFR}$, including for NGC 1614 (A. Adamo et al. 2020). Our calculated Γ_{1-10} in NGC 1614 is nearly four times lower than the value of $\Gamma_{1-10} = 83.1\% \pm 15.2\%$ found by A. Adamo et al. (2020) for this galaxy (black x in Figure 11); this discrepancy —mostly caused by assumptions in SFR and details of the age-dating method—is discussed further in the Appendix. Note that A. Adamo et al. (2020) did not calculate Γ_{10-100} or $\Gamma_{100-400}$.

5.2.2. Cluster Disruption

The fraction of stars that remain in older clusters provides important constraints on the disruption of the clusters. As we believe that there has been a fairly consistent star formation history in NGC 1614, we can compare values of $\Gamma_{1-10\,\rm Myr}$ with Γ_{10-100} and $\Gamma_{100-400}$ to probe the dissolution of clusters within NGC 1614. We find $\Gamma_{10-100} = 4.2\% \pm 1.1\%$ and $\Gamma_{100-400} = 1.4\% \pm 0.4\%$. These values show that the mass of stars in clusters decreases significantly, indicating that clusters begin to disrupt soon after they are born, continuing for at least the first $\sim$0.5 Gyr.

The shape of the cluster age distribution in NGC 1614 supports this picture of early, continuous cluster disruption. As shown in Figure 10, the age distributions of clusters in NGC 1614 are fairly similar in shape across the different mass intervals while staying above the completeness limit. The declining shape starts soon after formation, with a power-law index of $\gamma \approx -0.5$ for all plotted masses. A power-law index of -0.5 indicates that $\approx$70% of clusters are disrupted each factor of 10 in age. We do not see evidence of lower-mass clusters being disrupted earlier than higher-mass ones through the first $\sim$0.5 Gyr that we study here. Our estimates for Γ and the shape of the cluster age distribution agree with those found in previously published works for other star-forming galaxies (R. Chandar et al. 2017; D. O. Cook et al. 2023).

Our $\Gamma_{10-100} = 4.2\% \pm 1.1\%$, and $\Gamma_{100-400} = 1.4\% \pm 0.4\%$ values again agree well with the relation over a range in galaxies found by R. Chandar et al. (2017) of $\Gamma_{10-100} = 4.6\% \pm 2.5\%$ and $\Gamma_{100-400} = 2.4\% \pm 1.1\%$, shown in Figure 11. D. O. Cook et al. (2023), in a binned sample of more than 20 nearby dwarf galaxies, only calculated $\Gamma_{10-100} = 7\% \pm 2\%$, which is also in agreement with our calculated value. R. Chandar et al. (2023b) found ranges of $\Gamma_{10-100} = 5\%$–8% and $\Gamma_{100-400} = 1\%$–2% for their three blue compact dwarf galaxies.

5.3. Constraints on Ages in the UV-bright Arm

Star-forming clumps, often referred to as "star-forming complexes," have roughly kiloparsec sizes and can be seen in galaxies out to redshifts of $z = 4$–5, although substructure and individual clusters cannot be resolved at these distances (B. G. Elmegreen & D. M. Elmegreen 2005; D. M. Elmegreen et al. 2009; Y. Guo et al. 2015, 2018). High-redshift clumps tend to be very massive, $\sim10^8$–$10^9 M_\odot$ which is $\sim100\times$ higher than in local, noninteracting galaxies (D. M. Elmegreen et al. 2009). However, local interacting galaxies, like the Antennae (B. C. Whitmore et al. 2010), show signs of higher SFRs and larger cluster and clump sizes.

In the local universe, star-forming clumps have different properties in interacting versus noninteracting galaxies. In a study of more than 1000 clumps selected from 8 μm Spitzer images across 46 interacting and 38 noninteracting spirals within 70 Mpc, J. Zaragoza-Cardiel et al. (2018) found that clumps in interacting galaxies have higher $\Sigma_{\rm SFR}$ and younger ages than those in noninteracting galaxies, based on integrated photometry SED fitting of the clumps in the NUV through IR. From the CCDG HST sample of nearby interacting galaxies and blue compact dwarfs, D. M. Elmegreen et al. (2021) found $\sim$50 clumps across the sample after degrading the observations to mimic galaxies at up to $z = 2$. SED-based estimates for the clumps at low redshift found an average age of $\sim$180–500 Myr.

The UV-bright arm on the west side of the late-stage merger NCG 1614 shows little to no Hα emission and therefore has not been experiencing star formation for at least the past $\approx$10 Myr. The brightest region covers $\approx$4 kpc^2, outlined in Figure 12, and is representative of clumps found in galaxies at higher redshift (D. M. Elmegreen et al. 2021). The clusters identified in this region are circled in magenta and have colors that closely follow the BC03 solar-metallicity track, indicating that they experience little reddening. The colors indicate that massive clusters formed mostly $\sim$250–50 Myr ago, shown by the dashed vertical lines in the right panel of Figure 12. We find the median age of this region to be $\log(\tau/\rm yr) = 7.79$ ($\sim$60 Myr) with a standard deviation of 0.28 for clusters brighter than $m_V = 23$ mag within the contours shown in Figure 12. Median $V-I$ and NUV – B colors are found to be 0.68 and -1.1 mag, respectively, and are shown as the magenta diamond in

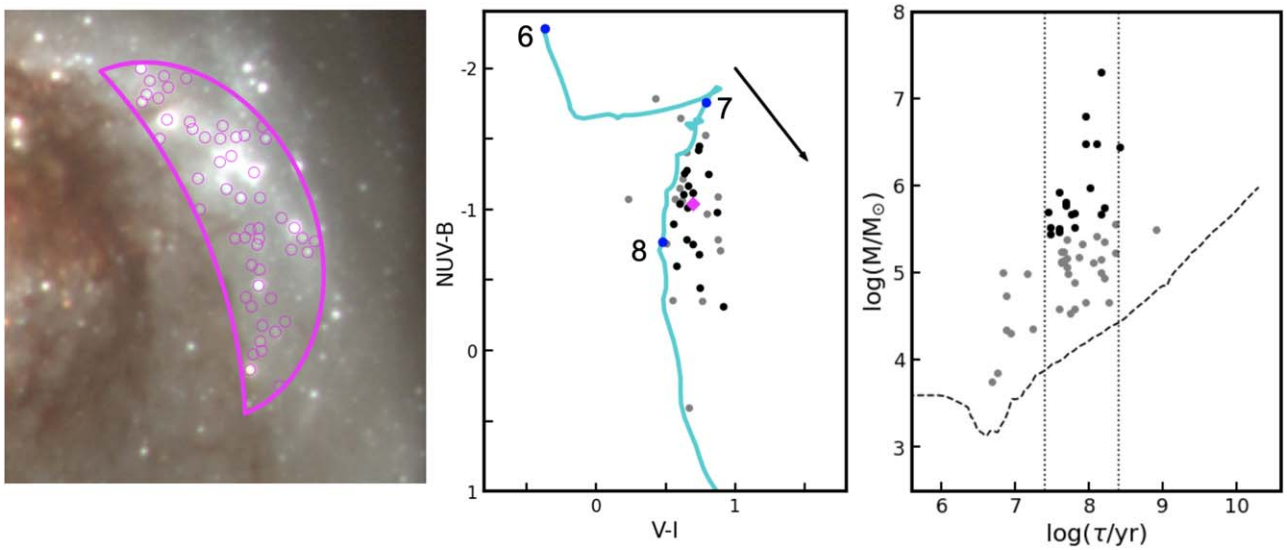

Figure 12. Clusters in the UV-bright arm of NGC 1614. Left: BVI HST color image with clusters identified by the magenta circles. Middle: NUV – B vs. $V - I$ color–color diagram of clusters brighter than $m_V \leqslant 23$ shown in black. The median color of these clusters is shown as the magenta diamond. An $A_V = 1.0$ reddening vector is shown in the upper right corner. Right: age–mass diagram of clusters within the UV-bright arm. The vertical dashed lines are at 25 and 250 Myr.

Figure 12. There is one very bright cluster in this region with an estimated mass around $10^7\,M_\odot$; the total mass of clusters with $M \geqslant 10^5\,M_\odot$ is $\sim 5.0 \times 10^7\,M_\odot$.

The duration of star and cluster formation in the UV-bright arm in NGC 1614 appears similar to that for hinge clumps, which are usually found in the tidal features of merging galaxies. B. J. Smith et al. (2014) found sustained star formation in hinge clumps of five nearby interacting galaxies, occurring either in multiple bursts or for a significant duration, rather than in a single, short-lived burst. This analysis was based on multiwavelength observations from the far-UV through X-ray, including Hα line strength. The prolonged star formation in hinge clumps is likely due to a prolonged inflow of gas. Massive clusters in the UV-bright arm of NGC 1614 have an age spread of $\approx$200 Myr, indicating that star formation in this region was also prolonged rather than a single, short-lived burst.

6. Summary and Conclusions

In this work, we studied the star cluster population in the LIRG NGC 1614 using HST photometry in eight bands: NUV (F275W), U (F336W), B (F438W), V (F555W), Hα (F665N), I (F814W), Paβ (F130N), and H (F160W). A key goal was to obtain accurate age, reddening, and mass estimates for the clusters, which requires successfully breaking the age–reddening degeneracy, as a means to allow for a cluster population analysis of the rest of the CCDG sample. We used an updated method to break this degeneracy, utilizing a comparison of predicted and observed SEDs of clusters in the six optical bands, including the narrowband Hα, in which we scale the maximum $E(B-V)$ allowed during the fitting procedure by the amount of dust in the region.

1. The distributions of cluster colors in NGC 1614, as seen in Figures 3 and 5, are found to be fairly continuous and show a range of reddening in different locations, from very low in the UV-bright arm to an $E(B-V) \approx 2.0$ mag in the dusty central region.
2. The most massive clusters have $M \approx$ few $\times\, 10^7\,M_\odot$, comparable to those found in other extreme systems, like the Antennae.
3. No statistically significant high-mass cutoff in the CMF was found. In addition, maximum likelihood fits of cluster masses for all studied age intervals (1–10 Myr, 10–100 Myr, 100–400 Myr) are found to be well fitted by a power law of approximately -1.8 and do not show statistically significant evidence for a Schechter-like upper mass cutoff.
4. The fraction of stellar mass born in clusters was calculated from the 1−10 Myr clusters and found to be $\Gamma_{1-10} = 22.4\% \pm 5.7\%$. This value is similar to values found for galaxies with $\Sigma_{\rm SFR}$ values $\sim$1000 times lower than that of NGC 1614.
5. The fractions of stars that remain in clusters surviving to ages of 10–100 Myr and 100–400 Myr are found to be $\Gamma_{10-100} = 4.5\% \pm 1.1\%$ and $\Gamma_{100-400} = 1.7\% \pm 0.4\%$, respectively. These results indicate that cluster disruption begins soon after the clusters form and continues for at least the first $\sim$0.5 Gyr.
6. The early, rapid dissolution of clusters is supported by the age distribution, which can be described by a simple power law with an index $\approx -0.5 \pm 0.1$ for clusters with masses greater than $10^5\,M_\odot$ up to ages of at least $\approx$0.5 Gyr.
7. The UV-bright arm has properties similar to stellar clumps observed in galaxies at redshift $z \approx 2$ and experienced fairly constant star formation for a period of $\approx$200 Myr starting 250 Myr ago.

Acknowledgments

R.C. acknowledges support from HST-GO-15649, and we thank the anonymous referee for suggestions that improved our manuscript. The HST data presented in this article were obtained from the Mikulski Archive for Space Telescopes (MAST) at the Space Telescope Science Institute. The specific

observations analyzed can be accessed via 10.17909/3yqt-mh67.

Software: Photutils (L. Bradley et al. 2020), Matplotlib (J. D. Hunter 2007), NumPy (T. E. Oliphant 2006; S. Van Der Walt et al. 2011), Astropy (Astropy Collaboration et al. 2022), APLpy (T. Robitaille & E. Bressert 2012) SciPy (P. Virtanen et al. 2020), SAOImage DS9 (Smithsonian Astrophysical Observatory 2000).

Appendix
The Dependence of Γ on Assumptions

The fraction of stars born in clusters, Γ_{1-10}, gives a key insight into how efficient the cluster formation process is in different star-forming environments. Γ is defined as

$$\Gamma = \frac{\text{Mass of Stars in Clusters}}{\text{Mass of All Stars}}, \quad \text{(A1)}$$

where the denominator, the total mass in stars, is simply calculated from the SFR multiplied by the age interval. The numerator, the mass of stars found in clusters, is calculated in two parts from (1) the sum of all masses of observed clusters above the completeness limit (within the age bin; see Section 4.2) plus (2) the total mass calculated by integrating a power law with index $\beta = -2$ over the mass range from $100\,M_\odot$ up to the cluster completeness limit (see Section 4.4 for more details).

The calculation of Γ relies on a number of assumptions that can drastically affect the result in some cases, and therefore the physical interpretation. Here we explore the different assumptions that have led to different estimates of Γ_{1-10} for NGC 1614.

One key assumption that can strongly affect Γ is the assumed SFR. Estimates of the SFR can vary widely for some galaxies, particularly those that have experienced unusual star formation histories, are interacting or merging, or have AGN activity. Dusty infrared-luminous galaxies in general can have a wide range of SFR estimates that depend on the tracer that is used. For example, published SFR estimates for NGC 1614 range from $27.4\,M_\odot\,\mathrm{yr}^{-1}$ (A. Adamo et al. 2020) to $74.7\,M_\odot\,\mathrm{yr}^{-1}$ (K. Tateuchi et al. 2015), or a factor of 2.7, which would translate to a factor of 2.7 difference in Γ. In this work, we assumed an SFR of $49.6\,M_\odot\,\mathrm{yr}^{-1}$, which is ≈factor of two higher than that assumed by A. Adamo et al. (2020), and therefore decreased our estimated Γ by a factor of two relative to theirs. Another example of very different estimates of the SFR for a galaxy are found for the late-stage merger NGC 34, which has experienced strong changes in its star formation history over the past ∼0.5 Gyr (Y. Zhang et al. 2024, in preparation). Published SFR estimates range between 5 and $90\,M_\odot\,\mathrm{yr}^{-1}$, or a factor of 18 (!), with hydrogen recombination lines giving much lower estimates than infrared-based tracers.

Other assumptions that can potentially impact Γ are related to the age-dating procedure itself. One key assumption, which we have explored in this work, is the maximum reddening value allowed during SED fitting to break the age–reddening degeneracy. We showed in Section 3.3 that many clusters that are older than 10 Myr can be incorrectly dated to younger than 10 Myr when the maximum $E(B-V)$ value allowed in the fit is too high. This age-dating problem has been identified in a number of other studies as well (e.g., R. Chandar et al. 2023b; B. C. Whitmore et al. 2023a). Age-dating issues can also affect cluster mass estimates. For example, the most massive cluster younger than 6 Myr (Hα bright) in NGC 1614 has an estimated mass that is 5 times higher in A. Adamo et al. (2020; who found $M = 1 \times 10^8\,M_\odot$) than that found here ($\sim 2 \times 10^7\,M_\odot$); their mass for this single cluster is 1.5 times more than the total mass we find for all 1–10 Myr clusters combined. Some reasons that cluster mass estimates might differ between different works are as follows: (1) the M/L_V changes by a factor of ∼2.5 for clusters with ages between 1 and 6 Myr (those predicted to have Hα emission), which means that mass estimates for young clusters can vary by a similar factor; and (2) clusters older than 10 Myr that are incorrectly fit to an age <10 Myr and moderate to high reddening will have artificially high mass estimates and be incorrectly included in the calculation for $\Gamma_{1-10\,\mathrm{Myr}}$.

We conclude that Γ is sensitive to details of the assumptions made to calculate it. Galaxies with very high rates of star formation and Σ_{SFR} in the nearby universe often have rapidly changing star formation histories, AGN activity, and a significant amount of dust, making calculations of Γ in these systems particularly challenging.

ORCID iDs

Miranda Caputo https://orcid.org/0000-0002-2957-3924
Rupali Chandar https://orcid.org/0000-0003-0085-4623
Angus Mok https://orcid.org/0000-0001-7413-7534
Sean Linden https://orcid.org/0000-0002-1000-6081
Paul Goudfrooij https://orcid.org/0000-0002-5728-1427
Bradley C. Whitmore https://orcid.org/0000-0002-3784-7032

References

Adamo, A., Kruijssen, J. M. D., Bastian, N., Silva-Villa, E., & Ryon, J. 2015, MNRAS, 452, 246
Adamo, A., Zeidler, P., Kruijssen, J. M. D., et al. 2020, SSRv, 216, 69
Astropy Collaboration, Price-Whelan, A. M., Lim, P. L., et al. 2022, ApJ, 935, 167
Bastian, N., Adamo, A., Gieles, M., et al. 2012, MNRAS, 419, 2606
Bradley, L., Sipőcz, B., Robitaille, T., et al. 2020, astropy/photutils: v1.0.0, Zenodo, doi:10.5281/zenodo.4044744
Bridge, C. R., Appleton, P. N., Conselice, C. J., et al. 2007, ApJ, 659, 931
Bruzual, G., & Charlot, S. 2003, MNRAS, 344, 1000
Calzetti, D., Lee, J. C., Sabbi, E., et al. 2015, AJ, 149, 51
Carpineti, A., Kaviraj, S., Hyde, A. K., et al. 2015, A&A, 577, A119
Chandar, R., Caputo, M., Linden, S., et al. 2023a, ApJ, 943, 142
Chandar, R., Caputo, M., Mok, A., et al. 2023b, ApJ, 949, 116
Chandar, R., Fall, S. M., Whitmore, B. C., & Mulia, A. J. 2017, ApJ, 849, 128
Chandar, R., Mok, A., French, K. D., Smercina, A., & Smith, J.-D. T. 2021, ApJ, 920, 105
Chandar, R., Whitmore, B., & Lee, M. G. 2004, ApJ, 611, 220
Chandar, R., Whitmore, B. C., Calzetti, D., & O'Connell, R. 2014, ApJ, 787, 17
Chandar, R., Whitmore, B. C., Dinino, D., et al. 2016, ApJ, 824, 71
Chandar, R., Whitmore, B. C., Kim, H., et al. 2010, ApJ, 719, 966
Conselice, C. J. 2014, ARA&A, 52, 291
Cook, D. O., Lee, J. C., Adamo, A., et al. 2019, MNRAS, 484, 4897
Cook, D. O., Lee, J. C., Adamo, A., et al. 2023, MNRAS, 519, 3749
Dinnbier, F., Kroupa, P., & Anderson, R. I. 2022, A&A, 660, A61
Dorn-Wallenstein, T. Z., & Levesque, E. M. 2018, ApJ, 867, 125
Eldridge, J. J., & Stanway, E. R. 2009, MNRAS, 400, 1019
Elmegreen, B. G., & Elmegreen, D. M. 2005, ApJ, 627, 632
Elmegreen, D. M., Elmegreen, B. G., Marcus, M. T., et al. 2009, ApJ, 701, 306
Elmegreen, D. M., Elmegreen, B. G., Whitmore, B. C., et al. 2021, ApJ, 908, 121
Engelbracht, C. W., Rieke, G. H., Gordon, K. D., et al. 2008, ApJ, 678, 804
Fall, S. M., & Chandar, R. 2012, ApJ, 752, 96
Fitzpatrick, E. L. 1999, PASP, 111, 63
Floyd, M., Chandar, R., Whitmore, B. C., et al. 2024, AJ, 167, 95

Forbes, D. A., Ferre-Mateu, A., Gannon, J. S., et al. 2022, MNRAS, 512, 802
Fouesneau, M., Lançon, A., Chandar, R., & Whitmore, B. C. 2012, ApJ, 750, 60
Gaia Collaboration, Brown, A. G. A., Vallenari, A., et al. 2018, A&A, 616, A1
Gieles, M., Bastian, N., Lamers, H. J. G. L. M., & Mout, J. N. 2005, A&A, 441, 949
Giménez-Arteaga, C., Brammer, G. B., Marchesini, D., et al. 2022, ApJS, 263, 17
Goddard, Q. E., Bastian, N., & Kennicutt, R. C. 2010, MNRAS, 405, 857
Goudfrooij, P., & Asa'd, R. S. 2021, MNRAS, 501, 440
Grudić, M. Y., Guszejnov, D., Offner, S. S. R., et al. 2022, MNRAS, 512, 216
Grudić, M. Y., Hafen, Z., Rodriguez, C. L., et al. 2023, MNRAS, 519, 1366
Grudić, M. Y., Kruijssen, J. M. D., Faucher-Giguère, C.-A., et al. 2021, MNRAS, 506, 3239
Guo, Y., Ferguson, H. C., Bell, E. F., et al. 2015, ApJ, 800, 39
Guo, Y., Rafelski, M., Bell, E. F., et al. 2018, ApJ, 853, 108
Herrero-Illana, R., Alberdi, A., Pérez-Torres, M. Á, et al. 2017, MNRAS, 470, L112
Hunter, J. D. 2007, CSE, 9, 90
Johnson, L. C., Seth, A. C., Dalcanton, J. J., et al. 2016, ApJ, 827, 33
Johnson, L. C., Seth, A. C., Dalcanton, J. J., et al. 2017, ApJ, 839, 78
Kennicutt, R. C., & Evans, N. J. 2012, ARA&A, 50, 531
Kruijssen, J. M. D. 2012, MNRAS, 426, 3008
Krumholz, M. R., McKee, C. F., & Bland-Hawthorn, J. 2019, ARA&A, 57, 227
Lee, J. C., Whitmore, B. C., Thilker, D. A., et al. 2022, ApJS, 258, 10
Leitherer, C., Schaerer, D., Goldader, J. D., et al. 1999, ApJS, 123, 3
Li, H., Gnedin, O. Y., & Gnedin, N. Y. 2018, ApJ, 861, 107
Li, H., Gnedin, O. Y., Gnedin, N. Y., et al. 2017, ApJ, 834, 69
Linden, S. T., Evans, A. S., Armus, L., et al. 2023, ApJL, 944, L55
Linden, S. T., Evans, A. S., Rich, J., et al. 2017, ApJ, 843, 91
Maraston, C. 2005, MNRAS, 362, 799
Maschmann, D., Lee, J. C., Thilker, D. A., et al. 2024, ApJS, 273, 14
Messa, M., Adamo, A., Calzetti, D., et al. 2018, MNRAS, 477, 1683
Modjaz, M., Kewley, L., Bloom, J. S., et al. 2011, ApJL, 731, L4
Mok, A., Chandar, R., & Fall, S. M. 2019, ApJ, 872, 93
Murphy, E. J., Bremseth, J., Mason, B. S., et al. 2012, ApJ, 761, 97
Oliphant, T. E. 2006, A Guide to NumPy, Vol. 1 (USA: Trelgol Publishing)
Portegies Zwart, S. F., McMillan, S. L. W., & Gieles, M. 2010, ARA&A, 48, 431
Randriamanakoto, Z., Vaisanen, P., Ryder, S., et al. 2013, MNRAS, 431, 554
Robitaille, T., & Bressert, E., 2012 APLpy: Astronomical Plotting Library in Python, Astrophysics Source Code Library, ascl:1208.017
Schlafly, E. F., & Finkbeiner, D. P. 2011, ApJ, 737, 103
Smith, B. J., Soria, R., Struck, C., et al. 2014, AJ, 147, 60
Smithsonian Astrophysical Observatory, 2000 SAOImage DS9: A Utility for Displaying Astronomical Images in the X11 Window Environment, Astrophysics Source Code Library, ascl:0003.002
Speagle, J. S., Steinhardt, C. L., Capak, P. L., & Silverman, J. D. 2014, ApJS, 214, 15
Tateuchi, K., Konishi, M., Motohara, K., et al. 2015, ApJS, 217, 1
Van Der Walt, S., Colbert, S. C., & Varoquaux, G. 2011, CSE, 13, 22
Virtanen, P., Gommers, R., Oliphant, T. E., et al. 2020, NatMe, 17, 261
Whitmore, B. C., Chandar, R., Lee, J., et al. 2020, ApJ, 889, 154
Whitmore, B. C., Chandar, R., Lee, J. C., et al. 2023a, MNRAS, 520, 63
Whitmore, B. C., Chandar, R., Rodríguez, M. J., et al. 2023b, ApJL, 944, L14
Whitmore, B. C., Chandar, R., Schweizer, F., et al. 2010, AJ, 140, 75
Zackrisson, E., Rydberg, C.-E., Schaerer, D., Östlin, G., & Tuli, M. 2011, ApJ, 740, 13
Zaragoza-Cardiel, J., Smith, B. J., Rosado, M., et al. 2018, ApJS, 234, 35
Zhang, Q., & Fall, S. M. 1999, ApJL, 527, L81